ACS APPLIED MATERIALS & INTERFACES

www.acsami.org

Research Article

Ultrasparse View X-ray Computed Tomography for 4D Imaging

Yanjie Zheng and Kelsey B. Hatzell*

Cite This: *ACS Appl. Mater. Interfaces* 2023, 15, 35024−35033

Read Online

ACCESS | Metrics & More | Article Recommendations | Supporting Information

ABSTRACT: X-ray computed tomography (CT) is a noninvasive, nondestructive approach to imaging materials, material systems, and engineered components in two and three dimensions. Acquisition of three-dimensional (3D) images requires the collection of hundreds or thousands of through-thickness X-ray radiographic images from different angles. Such 3D data acquisition strategies commonly involve suboptimal temporal sampling for *in situ* and *operando* studies (4D imaging). Herein, we introduce a sparse-view imaging approach, Tomo-NeRF, which is capable of reconstructing high-fidelity 3D images from <10 two-dimensional radiographic images. Experimental 2D and 3D X-ray images were used to test the reconstruction capability in two-view, four-view, and six-view scenarios. Tomo-NeRF is capable of reconstructing 3D images with a structural similarity of 0.9971−0.9975 and a voxel-wise accuracy of 81.83−89.59% from 2D experimentally obtained images. The reconstruction accuracy for the experimentally obtained images is less than the synthetic structures. Experimentally obtained images demonstrate a similarity of 0.9973−0.9984 and a voxel-wise accuracy of 84.31−95.77%.

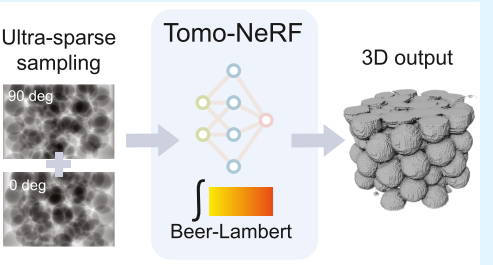

KEYWORDS: *sparse reconstruction, X-ray computed tomography, tomographic reconstruction, neural radiance field, operando imaging*

INTRODUCTION

X-ray computed tomography (XCT) tools are noninvasive imaging tools that can capture subsurface morphological and structural features in a range of materials and material systems.[1] The fidelity of microstructure representation is essential for material property estimation, simulation, and materials design.[2] Three-dimensional reconstructions of materials are often utilized to accurately model components and critically assess degradation and material transformation pathways.[3] The resiliency of any quantitative assessment is highly dependent on the reconstruction of a three-dimensional (3D) image from hundreds of 2D radiographic images acquired from different projection angles.[4,5] The inverse Radon transform provides the mathematical basis for the conventional reconstruction process.[6] Hundreds of 2D images at varying angles are typically acquired in order to reconstruct images into a 3-D rendering. For dynamic or *operando* investigations, where you combine an action with imaging (*e.g.*, imaging particles flowing), it is challenging to take hundreds of images in the time period of the action. Thus, 3D imaging for *in situ* and *operando* studies, which require fast acquisition times on the order of seconds or subsecond per frame, are challenging.[7] Sparse-view reconstruction approaches attempt to reduce the number of 2D images (*e.g.*, sampling rate) necessary for 3D reconstruction.[8−12] Decreasing the sampling rate enables transient *in situ* and *operando* studies. Reducing the number of images needed for a reconstruction can have the added benefit of less instrument maintenance, longer system lifetime, and simpler system design and hardware.[13] Despite the promising features, sparse-view reconstruction *via* conventional reconstruction methods suffers from the inevitable information loss that hinders correct image interpretation and quantification.

Image reconstruction in computed tomography has undergone a paradigm shift as a result of recent advancements in deep learning for computer vision applications.[14] However, unlike tomographic slice reconstruction in biomedical fields,[13] microscopic computed tomography in materials studies is limited by training data sets. The region of interest for micro/mesostructure studies can be orders of magnitude smaller than in biomedical and clinical studies. This significantly lengthens data acquisition periods and necessitates access to a synchrotron source with a brilliance a billion times brighter than a laboratory source.[15] Reconstruction of 3D images from high-dimensional 2D data sets is another challenge. The two primary methodologies of deep sparse-view reconstruction are image quality enhancement[13] and stochastic reconstruction.[2] The former adapts deep learning networks to reduce noise and strike artifacts from the sparse-view reconstruction. The networks in the data domain interpolate missing sinogram data (*i.e.*, Radon transform data) of sparse-view reconstruction by learning from complete projection sinograms.[3,16−20] The networks in the image domain restore the image quality by

Received: May 2, 2023
Accepted: June 28, 2023
Published: July 13, 2023

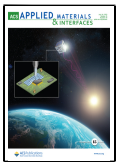

learning to detect and subtract streak-type artifacts from the undersampled reconstruction images.[21,22] Either by learning from data or images, these deep learning models incorporate analytical transform (*e.g.*, Radon transform) as physical-based knowledge for image reconstructions, cutting the number of projection views needed from hundreds to dozens. However, these methods still face the bottleneck of reconstructing images from single-digit views since they need enough views to perform the reconstruction *via* the Radon transform for further quality enhancement. An alternative approach is stochastic reconstruction. Stochastic reconstruction utilizes deep convolutional generative adversarial networks (GANs) as layered architecture to extract and reproduce the hierarchical features of image data sets.[2] From representative 2D CT scan slices, GANs may stochastically generate a statistically equivalent 3D structure of porous media,[23] three-phase electrodes,[2,24] and anisotropic polymer membranes.[2] The synthetic volumes *via* stochastic approaches demonstrate statistical similarity with the original data sets, while they cannot reveal the real 3D structure from the input 2D images. The loss of localized geometric information is inevitable. Therefore, they are ineffective for transient *in situ* and *operando* studies or heterogeneity studies, where realistic variations in localized properties across time or space matter.

Ultrasparse view 3D tomography reconstruction with deep learning methods is an underexplored area due to model limitations and insufficient training data. Herein, we introduce a learnable framework capable of reconstructing high-fidelity 3D images from single-digit radiographic images (Tomo-NeRF). Tomo-NeRF is distinct from the quality enhancement and stochastic reconstruction methods and does not rely on the analytical knowledge of inverse transform for reconstruction. Instead, Tomo-NeRF is a physics-based approach which utilizes the Beer−Lambert law to reconstruct samples. Enlightened by pixel-NeRF,[25] a photorealistic novel view synthesis model, Tomo-NeRF aligns pixel and voxel in the 3D coordinate system *via* relating the X-ray attenuation to the material properties of the sample. The algorithm learns to predict the phase of each voxel with the grayscale value from 2D radiographic images. We train the model with a set of multiview radiography projections along with the 3D voxel labels so that the model can learn the scene prior to reconstruction from two-view radiographic images. Obtaining thousands of 3D and 2D training data sets from real experiments for training is cost-prohibitive. Herein, we utilize a numerical simulator to create synthetic data. Synthetic reconstructions are combined with physics-based equations (*e.g.*, Beer−Lambert) to generate artificial radiographic images for the 2D training data sets. To demonstrate the functionality of Tomo-NeRF and the artificial training data sets, we conduct real full-view tomography imaging experiments on granular ceramic proppants with monodispersed sizes. These ceramic proppants are made of bauxite and are commonly utilized for high-temperature heat transfer from concentrated solar power plants. The bauxite particle heat exchangers are comprised of spheroid materials which can exhibit a range of aspect ratios and varying morphologies. By combining synthetic data with experimental data we can test Tomo-NeRF's ability reconstruct 3D images from less than 10 views.

TOMO-NERF

Tomo-NeRF is a learning framework that can reconstruct 3-D images from a limited number of fixed radiographic projection views. Neural radiance field (NeRF) was previously developed for novel photorealistic view synthesis with an incomplete set of photos.[26] It leverages a continuous volumetric radiance field of color and density for volumetric scene prediction and uses gradient descent to optimize the scene using the input photos. Our Tomo-NeRF employs the convolutional approach to the conventional NeRF, pixelnerf.[25] Convolutional layers in convolutional neural networks (CNNs) utilize a local receptive field defined by the size of the convolutional kernel.[27] This design enhances network's flexibility and computational efficiency when extracting image features, compared to a fully connected structure. Therefore, CNNs would be more suitable for computed tomography reconstruction in tolerating potential noise within the input radiographic images. To realize the ultrasparse view reconstruction in X-ray computed tomography, we embed the physical field of X-ray imaging into NeRF, making it correspond to real experiments.

Physical Field of X-ray Imaging. Radiographic images are 2D images which capture variable attenuation characteristics in a material or component.[28] An X-ray source emits fluxes of X-ray photons that pass through or interact with the sample.[29] Any interaction, *via* scattering or absorption, removes the photon from the X-ray beam.[30] The attenuation coefficient (μ) is a material property which describes how easily an X-ray can pass through a material. The attenuation coefficient of a material depends on the type of material (atomic number and density) and the photon energy of the radiation.[31] The X-ray attenuation often varies in space for heterogeneous materials comprised of either multiple materials or local variations in density. The detector electronically detects the photons that pass through the sample. Other than the material types and incident photon energy, the decrease in detected X-ray intensity is dependent upon the depth of X-ray beam penetration through the sample (*i.e.*, material heterogeneity).[30] The computer will further process the through-thickness projection data (*e.g.*, adjust brightness and contrast) and visualize it as a grayscale radiographic image. The Beer−Lambert law relates the X-ray beam attenuation to the material properties (attenuation coefficient) and the penetration depth (z). With a parallel-beam approximation, the general equation to calculate detected X-ray intensity I_d is

$$I_d(x, y) = \int_0^{\varepsilon_{max}} \eta(\varepsilon) I_0(\varepsilon) \exp\left(-\int \mu(x, y, z; \varepsilon) dz\right) d\varepsilon \quad (1)$$

where $\eta(\varepsilon)$ is the quantum efficiency of the detector and $I_0(\varepsilon)$ is the incident X-ray intensity with the unit of photons per unit area per unit electron energy (photons/(m^2 keV)). The incident X-ray intensity is a function of X-ray energy (ε). Variations in material properties are more detectable than variations in X-ray energies, particularly when utilizing a synchrotron facility that can generate an almost monochromatic X-ray source.[30] Therefore, Tomo-NeRF neglects the incident energy variation and simplifies the Beer−Lambert Law function as only an integral function of penetration thickness

$$I_d(x, y) = \eta \times I_0 \times \exp\left(-\int \mu(x, y, z) dz\right) \quad (2)$$

The Beer−Lambert law function allows for a continuous 3D field representation and aligns material microstructures in spatial location (x, y, z) with the radiographic projection on the 2D plane (x, y). The continuous volumetric representation allows for interpolating volumetric density from neighboring

https://doi.org/10.1021/acsami.3c06291
ACS Appl. Mater. Interfaces 2023, 15, 35024−35033

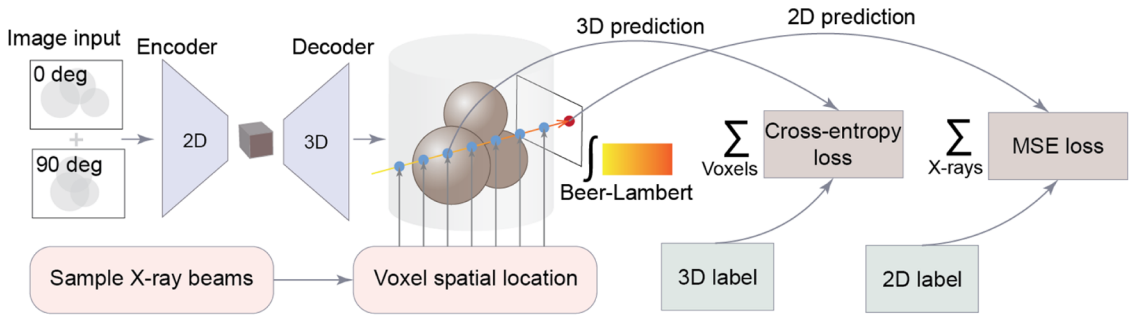

Figure 1. Overview of the Tomo-NeRF pipeline (memory size of the whole model is ~80 MB).

input views, providing additional depth information in the novel views. The additional information relaxes the Nyquist sampling bound of projection views required for conventional reconstruction in discrete representations.

X-ray computed tomography 3D reconstruction requires through-thickness information from different views (conventional methods would require hundreds of views). Therefore, the tomography imaging experiment involves radiographic scanning around a sample by fixing the X-ray source and detector and rotating the sample at a constant altitude around the central axis.[32] To represent spatial location of X-ray beams from different imaging directions, we encode the projection direction into a Cartesian coordinate system. We sample points along the 0° projection beam as a reference coordinate (x_0, y_0, z_0) and rotate the X-ray parallel beams in the reverse direction of the sample rotation. For a field of view of $w \times w$, the reference point (x_0, y_0, z_0) on X-ray parallel beams rotates angle θ around the central vertical axis (*i.e.*, y-axis) where (x_c, y_c) = ($w/2$, $w/2$) will be (x_1, y_1, z_0). Here,

$$x_1 = (x_0 - x_c)\cos(\theta) - (y_0 - y_c)\sin(\theta) + x_c \quad (3)$$

and

$$y_1 = (x_0 - x_c)\sin(\theta) - (y_0 - y_c)\cos(\theta) + y_c \quad (4)$$

Model Pipeline. Tomo-NeRF (Figure 1) utilizes an encoder−decoder convolutional neural network to extract features from images and align the features of the input image with 3D geometry in a voxel grid (see the Supporting Information). Tomo-NeRF uses a modified ResNet34 as a 2D encoder to extract local and global information from radiography images. A 3D decoder further processes the output feature vector from the 2D encoder with the upsampling methods of transposed convolution and bilinear interpolation. It reshapes and restores the feature vector into a 3D feature map that aligns with the 3D ground truth in the voxel grid. The last layer of the convolution neural network within the 3D decoder is a sigmoid activation function $S(x) = \frac{1}{1+e^{-x}}$ to bound the output between 0 and 1,[33] turning each voxel grid into a classifier. For a two-phase sample (*e.g.*, ceramic proppants), the numerical prediction in each voxel within the 3D feature map represents the probability prob of finding the solid phase in that spatial location. If prob > 0.5, the grid has a higher chance of being occupiedby a solid material (*e.g.*, ceramic), otherwise it is unoccupied (*e.g.*, air).

During the training process (see the Supporting Information), the encoder−decoder convolutional neural network takes the 0 and 90° projection images as the input and produces a 3D feature grid of probability information that matches the original size of the volumetric grid (100 × 100 × 150). The model samples voxel grids, along X-ray beams among the six projection directions (*i.e.*, beam rotation angle θ). Each direction ranges from 0 to 180° with a step of 30°. It sends the query specification of the spatial location along with the input image into the Tomo-NeRF network to retrieve the corresponding feature from the predicted 3D feature grid. The model compares the retrieved 3D prediction along the X-ray beam with the 3D ground truth and has a cross-entropy loss (L_{CE}) for each grid to learn from the 3D data set. Tomo-NeRF programs that each X-ray beam in the network may produce a grayscale pixel on the radiographic image under a given projection direction. Therefore, the model can further make a 2D prediction of the pixel value by integrating the 3D predictions on the specified X-ray beams with the Beer−Lambert law (eq 2). By comparing the 2D prediction (*i.e.*, a radiographic image from 3D predictions) with the radiography ground truth corresponding to its projection direction, the model can learn from the 2D data set (*i.e.*, six direction radiographic images for each sample) *via* mean-square-error (MSE) loss. By continuously minimizing cross-entropy (eq S2 in the Supporting Information) and MSE (eq S3 in the Supporting Information) losses during the training process, Tomo-NeRF can learn to increase the probability of predicting the voxel phase from 3D labels and six-views. Other than improving learning performance from 2D labels, the 2D prediction allows comparison with input images while optimizing the trained network, testing, or experimental validation, where 3D labels are unavailable. Learning from one projection direction can serve as relevance and share knowledge for other directions. The model can rely more directly on the input image feature if the query projection direction and input orientation are similar; otherwise, the model needs to leverage the learned prior.

EXPERIMENTAL METHODS

Tomo-NeRF reconstruction capabilities were evaluated on a bauxite granular material. Granular media are commonly used for high-temperature heat transfer, catalysis, food, and pharmaceutical applications.[34,35] Understanding the kinetics of dense granular flow *via* a noninvasive method is essential to flow phenomena studies (*e.g.*, Brazil nut effect,[36] pattern formation,[37] jamming transition,[38,39] local rearrangement,[40] *etc.*) and heat transfer analysis.[41,42] However, dynamic granular flow studies with a noninvasive method have been limited to radiographic studies due to the rate dependency in granular flow. Tomo-NeRF enables the prediction of complex 3D microstructures from a limited number of radiographic images.

X-ray microcomputed tomography imaging was conducted on a sintered bauxite proppant sample, which is typically used as a heat transfer and storage medium within particle-based concentrated solar power plants.[42] Here, we used CARBO HSP 16/30, a commercialized sintered bauxite proppant sample composed of Al_2O_3, SiO_2, TiO_2, and

https://doi.org/10.1021/acsami.3c06291
ACS Appl. Mater. Interfaces 2023, 15, 35024−35033

Table 1. Summary of Four Experiments with Input Data and Training Input Data for the Model

experiment #	input data	training data for the model
Experiment #1	real XCT	synthetic data—irregular spheres
Experiment #2	synthetic data—irregular sphere	synthetic data—irregular sphere
Experiment #3	synthetic data—regular sphere	synthetic data—regular sphere
Experiment #4	synthetic data—irregular sphere	synthetic data—regular sphere

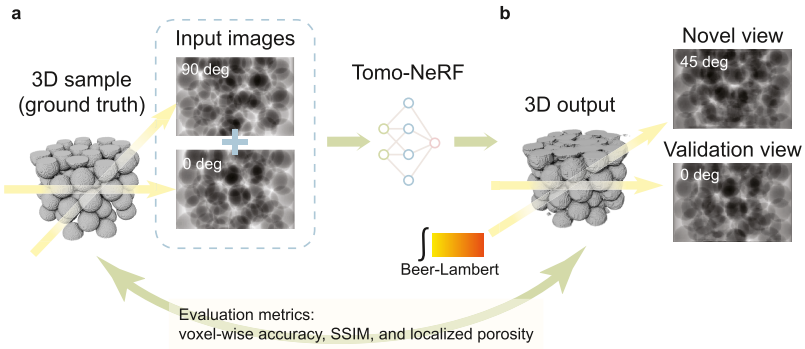

Figure 2. Example of a two-view reconstruction for an artificial sphere sample (in a voxel-wise accuracy of 90.39%) for illustrating the experimental workflow. (a) The artificial image generator first produces a 3D sample of identical sphere particles with a discrete element method simulator and then makes artificial radiographic images in 0 and 90° projecting direction. (b) Tomo-NeRF takes the concatenated two images as an input and predicts a 3D image. The Beer−Lambert law applies to the 3D output to make 2D radiographic projections in the same projection angle of input images as the validation view (*e.g.*, 0°) and the different projection angle as the novel view (*e.g.*, 45°).

Fe_2O_3. It is a monodispersed granular material with 85% of the particle equivalent diameters falling within the range of 850−1180 μm and 12% lower than 850 μm.[43] Each grain in the CARBO HSP 16/30 sample is irregular in shape, with a sphericity of 0.9. ZEISS Xradia Versa 3D X-ray microscopes probed the CARBO HSP 16/30 sample in a quartz tube (inner diameter of 3.95 mm and outer diameter of 4.95 mm) placed between the source and detector. The imaging field of view is 4085 μm × 4085 μm, slightly larger than the inner diameter of the container (3950 μm). The X-ray tube voltage that is relevant to photon energy is 60 kV. We applied a low-energy filter to make the X-ray beam closer to monochromatic. The exposure time for each radiographic imaging is 1.5 s. The microscope system has a full scan around the sample for 1600 projections for reconstructing a 3D tomographic image. To evaluate the Tomo-NeRF reconstruction capability in different numbers of projection views, we selected two projections (0 and 90°), four projections (0, 45, 90, and 135°), and six projections (0, 30, 60, 90, 120, and 150°) from the 1600 projections as the 2D input for the model. We obtained real tomographic (reconstruction from full view) and radiographic images as reference samples (*i.e.*, real sample) for evaluating reconstruction performance.

Training Tomo-NeRF requires thousands of 2-D and 3-D image training data sets for an accurate reconstruction. Acquisition of such a large number of real data sets faces the limitations of time, cost, and synchrotron source availability. Herein, we propose an artificial image generator as a means for obtaining an affordable training data set. For preparing 3-D artificial samples, we utilized a discrete element method simulator[44] to randomly assemble packs of grains in a cylinder container based on physical forces. The artificial data set closer to the real samples will benefit the training performance. The information on the particle size distribution and irregularity (relevant to Perlin noise altitude[44]) enables the simulator to generate artificial 3D structures of irregular shapes that resemble the real samples. The simulator produces the packed bed shape structures in terms of TIFF files. Each TIFF file contains a 3-D binary matrix of structure information that distinguishes each voxel into ceramic or air. The structure and materials of the real-experiment container are known properties. Therefore, we can mathematically create randomly assembled particle-packed beds in quartz containers as the artificial tomography images. For preparing the corresponding 2-D radiographic images, we leverage the fundamental principle of X-ray radiographic imaging. The Beer−Lambert law indicates that the detected X-ray intensity $I_d(x, y)$ corresponds to the material structure and properties in 3D space (x, y, z) at known X-ray source properties. We are able to estimate the attenuation coefficient with a quartz density of 2.6 g/cm^3 and a ceramic density of 3.61 g/cm^3.[45] The attenuation coefficient in the real experiment might deviate from the expected one due to the difference in incident energy and material properties. The potential deviation is acceptable as long as the attenuation difference among the ceramic, quartz, and air is large enough to form the extractable features on radiographic images. In addition, the model normalizes the input images during preprocessing. With the 3-D structure and corresponding properties, we are able to integrate the attenuation coefficient μ along the X-ray beams in the z-direction. The generator further mathematically rotates the 3-D structure along the central y-axis every 30° for generating radiographic images in six different views.

The artificial image generator prepares two different types of data sets: (1) synthetic data with regular spheres and (2) synthetic data with irregular spheres (nonsmooth). The first type of data set is randomly packed identical spherical particles with 600 μm diameter in a 3 mm inner diameter tube (*i.e.*, artificial sphere sample). The second data set is randomly packed monodispersed particles in a 3.95 mm inner diameter tube. The irregular spheres more closely resemble the real bauxite materials (*e.g.*, ceramic proppant) used in the experimental tomography imaging experiment.

To validate the reconstruction capabilities of Tomo-NeRF, we conduct four deep learning experiments (Table 1). Each experiment used a specific type of synthetic data set as the training data and a specific input to test the algorithm's ability to convert two-, four-, and six-views into a 3D image. Two-view means two radiographic images taken from two different angles, while six-view means six radiographic images taken from six different angles. Conventional tomography combines 1000 s of radiographs from 1000 s of different angles to create 3-D images. All input data sets were original and were not utilized in the training process. Experiment #1 uses real X-ray radiographic images of the bauxite particles as an input for the model trained with synthetic data comprised of irregular spheres (non-smooth). The first experiment specifically aims to evaluate the practicality of the proposed Tomo-NeRF in real XCT applications. Experiments #2 and #3 use the synthetic data as the input data and utilize algorithms trained with their respective types of data sets

https://doi.org/10.1021/acsami.3c06291
ACS Appl. Mater. Interfaces 2023, 15, 35024−35033

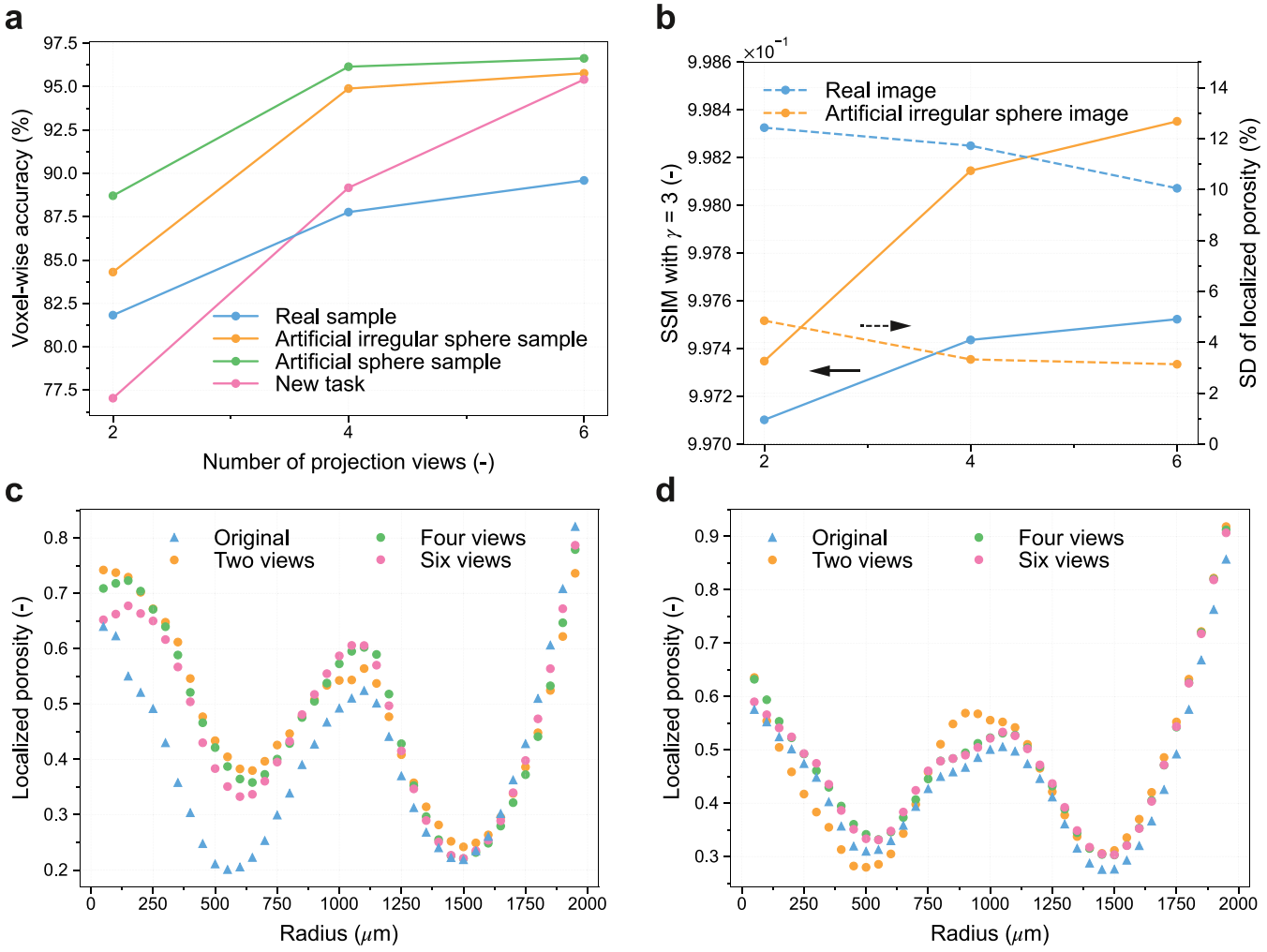

Figure 3. (a) Reconstruction voxel-wise accuracy increases with more available input projection views, and the new task samples have the highest increasing rate. (b) Structural similarity (SSIM) with exponent for the structural term (γ) of 3 exceeds 0.997, and it increases with more input views. The standard deviation (SD) of localized porosity decreases with more views. (c) The localized porosity radial profile from the center to the near-wall region for the real sample (voxel-wise accuracy ranges from 81.83 to 89.59%) shows that the major deviations occur near the central region. (d) The localized porosity radial profile for the artificial sample (voxel-wise accuracy ranges from 86.40 to 95.37%) has a smaller deviation than the real sample.

(Table 1). These experiments aim to validate the feasibility of the proposed Tomo-NeRF's reconstruction principle and to investigate the role of geometric complexity (*e.g.*, uniform *vs* irregular spheres) on the reconstruction results. Experiment #4 utilizes radiographic images of artificial irregular sphere samples into the model trained by the artificial spherical shape sample data set. Tomo-NeRF takes the two-view, four-view, or six-view images as the input (Figure 2a) and reconstructs a 3-D image as the output (Figure 2b). We visualize the 2-D prediction images by further making projections on the 3-D output in both the same and different directions of the input images (*i.e.*, validation view and novel view). The quality of the novel view from 2-D prediction represents the model reconstruction capability when there is a lack of information in a direction different from the input image. Other than visual comparison, we quantitively evaluate the reconstruction accuracy with 3-D structural similarity (SSIM), voxel-wise accuracy, and the standard deviation of localized porosity (see the Supporting Information) by using the 3D ground truth sample as the reference.

RESULTS

The reconstruction accuracy increases with an increasing number of input views for each of the four experiments (Figure 3a). The rate of improvement decreases for Experiments #1, #2, and #3 but steadily increases for Experiment #4. Experiment #3 which uses uniform spheres as an input and an algorithm trained on synthetic data with uniform spheres has the highest accuracy across all number of views. Eight synthetic samples in the testing process have an average accuracy of 88.71% in two-view reconstruction, and this increases to 96.63% with six-input views. It is unsurprising that Tomo-NeRF performs better in reconstructing images with smooth and predictable surfaces and regular sizes (*e.g.*, uniform spheres). Reconstructing "real XCT" data (Experiment # 1) results in lower reconstruction accuracy. The real X-ray data set has voxel-wise accuracy around 81.83, 87.77, and 89.59% for two-view, four-view, and six-view reconstructions, respectively. The fourth experiment, which incorporates irregular shaped spheres into a model trained for regular spheres has the lowest reconstruction accuracy with 2 views. However, the fourth experiment shows the greatest improvement in voxel-wise accuracy with increasing projection views.

Similar to the voxel-wise accuracy, the trend for structural similarity (SSIM) increases with the number of projection views (Figure 3b) for the real XCT data (*e.g.*, Experiment #1)

https://doi.org/10.1021/acsami.3c06291
ACS Appl. Mater. Interfaces 2023, 15, 35024−35033

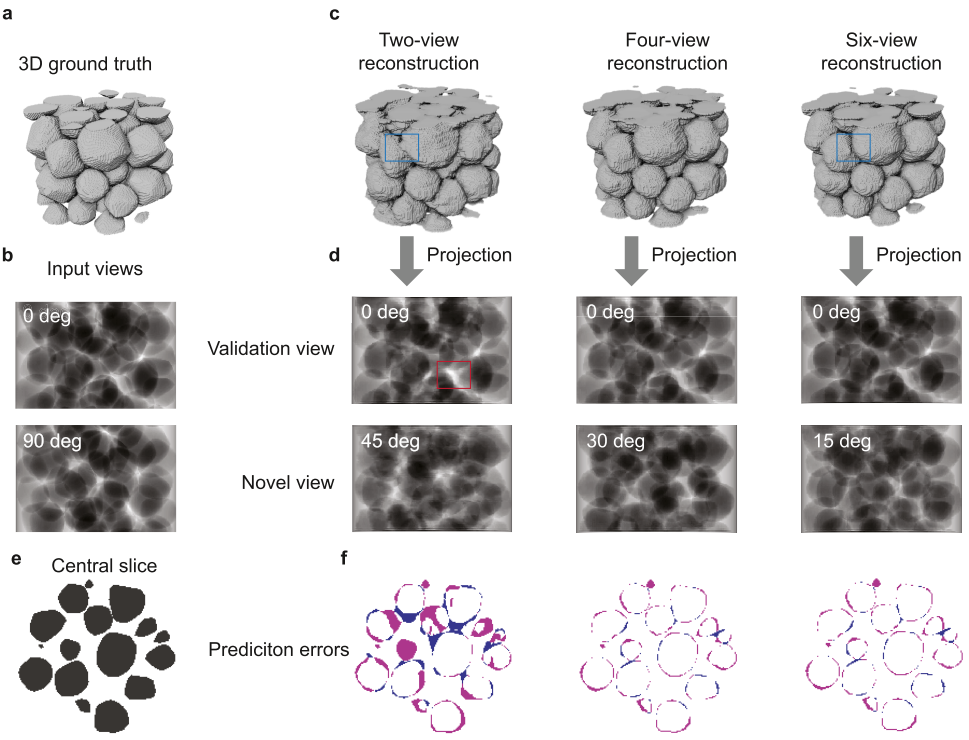

Figure 4. (a) 3D ground truth of an example of the synthetic sample of irregular shape (Experiment #2). (b) Input view examples in 0 and 90°. (c) 3-D visualization of two-view, four-view, and six-view predictions. There is less adhesion between some of the particles as more input views (blue box). (d) The validation views exhibit a strong overall structural similarity to the input view. In the two-view reconstruction, there is a high-contrast region that has a marginally poor restoration of details (red box), and it gets improved with more input views. In the novel view visualizations, individual particle outlines becomes more distinct with more input views. (e) The central slice of ground truth. (f) Visualization of prediction errors on the central slice. Pink indicates that the prediction into the air for the actual phase is solid, and blue indicates that the prediction into solid for the actual phase is air. Prediction accuracy increases as the reconstruction views are above two. The prediction errors are evenly distributed around the surfaces of the particles.

and synthetic irregular spheres (*e.g.*, Experiment #2). Tomo-NeRF shows a high fidelity in structural restoration. When the input data is real XCT data, the two-view reconstruction has a low accuracy but the structural similarity (SSIM) still reaches as high as 0.9971. The highest value of structural similarity (SSIM) is 0.9984 for the six-view reconstruction of the artificial sample (*e.g.*, synthetic data with irregular spheres). Another way to evaluate the resiliency of the reconstruction is to extract local microstructure properties (*e.g.*, porosity) for the different particle beds. The porosity radial profile through the reconstructed sample was systematically compared for the true XCT data (*e.g.*, Experiment #1) and input data containing irregular spheres (*e.g.*, Experiment #2). Figure 3c,d demonstrates the radial porosity for input data (*e.g.*, original) and two-, three-, and six-view reconstructions. The real XCT data (*e.g.*, Experiment #1) demonstrates wide porosity variations between the different views (Figure 3c) and captures the subsurface variability in the learning exercise. The standard deviation of localized porosity distribution is between 3.14 and 4.85% for the synthetic data with irregular spheres (Figure 3d, Experiment #2) and 10.05−12.43% for the real XCT sample (Figure 3c, Experiment #1)

Synthetic data was constructed with irregular shaped spheres of varying sizes (*e.g.*, Experiment #2). The 3D ground truth (Figure 4a) and predicted images (Figure 4c) demonstrate that all of the reconstructions (two-, four-, and six-views) demonstrate similar packing densities as the ground truth. As the number of projection views increases, the details of the particles' shape are more accurate and the surface is smoother. The adhesion between some of the particles is attenuated since the reconstructed particles' shape is more accurately represented. The 2D predictions in the validation views (Figure 4d) show a high similarity to the input view (Figure 4b) at the same projection angle (0°) in all reconstructions except for the high-contrast particle overlapping region in the two-view reconstruction. The novel view projections define more clearly particle boundaries as the number of views increases to four (Figure 4d).

Similar to the synthetic sample with irregular particles, the reconstruction of the real XCT data appears more similar to the input data with higher input views (Figure 5c). However, the overall reconstruction quality is not as high as the artificial sample in Figure 4. The XCT data has more artifacts due to X-ray scattering and local variations in the material which leads to deviation between the assumptions of the model and artificial image generator. Tomo-NeRF and artificial image generators assume a monochromatic beam. In reality, synchrotron facilities produce monochromatic beams (I_0) through single-crystal monochromators and X-ray diffraction at a higher intensity than the in-house imaging facility in our experiment.[46] The in-house imaging facility uses the filter to decrease the intensity of the beams with an unwanted wavelength, yet the emitted radiation is still polychromatic, which is different from the ideal assumption (eq 2). This deviation results in an attenuation coefficient which is dependent on the local spatial heterogeneity in the sample and X-ray energy (*i.e.*, $\mu(x, y, z; \varepsilon)$). In addition, the lower energy of the in-house facility increases the contrast I_d/I_0 (*e.g.*, the overexposure for the void

https://doi.org/10.1021/acsami.3c06291
ACS Appl. Mater. Interfaces 2023, 15, 35024−35033

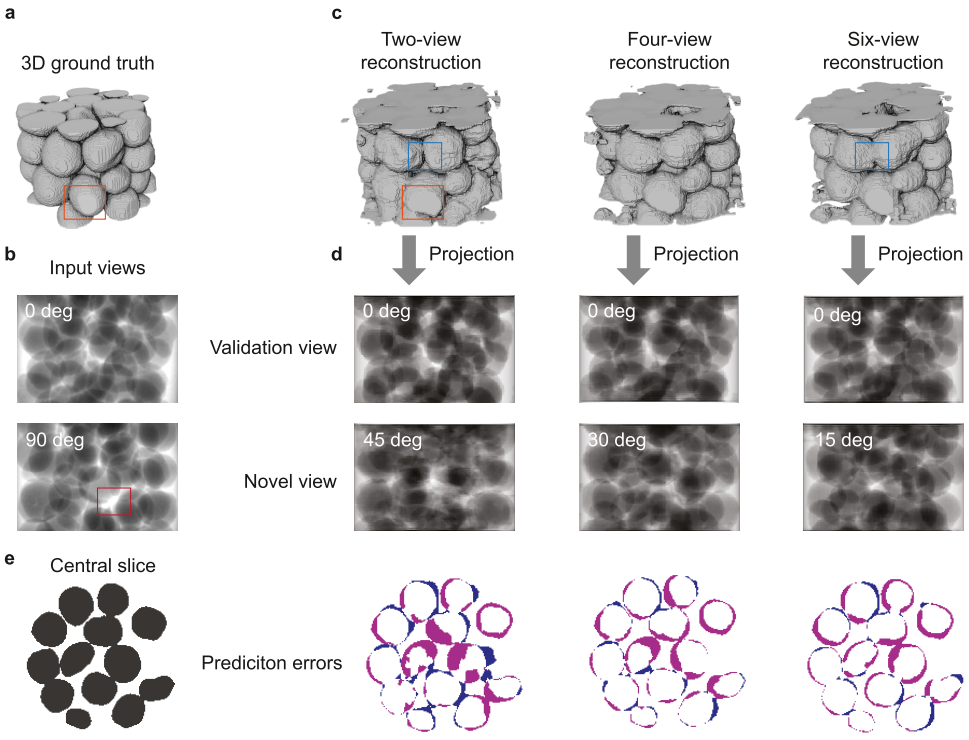

Figure 5. (a) 3D ground truth of tomographic image reconstructed from the full-view X-ray imaging experiment (Experiment #1). (b) Input view examples in 0 and 90°. The lower energy intensity and noise in the real in-house imaging experiment blur the outline of particles' projection on the radiographic images, resulting in information loss (red box). (c) 3D visualization of two-view, four-view, and six-view predictions. More input views tend to aggravate the particle adhesion (blue box). (d) The validation view shows a higher structural similarity to the input view with increasing views. In the novel view visualizations, the outline of particles' projection gets clearer with more input views. (e) The central slice of ground truth. (f) Visualization of prediction errors on the central slice. Pink indicates the prediction into the air for the actual phase is solid, and blue indicates the prediction into solid for the actual phase is air. Prediction accuracy increases as the reconstruction views are above two. The prediction error is unevenly distributed.

region near the overlapping particles) and results in more noise in the real experiment (Figure 5b). By comparing the input images from the real sample (Figure 5b) and that from the artificial samples (Figure 4b), we can see that there is information loss in the particle shape, where the boundaries of the overlapping particles cannot be resolved due to high contrast and noise. It is more difficult for the convolution network to extract features from blurrier input radiographic images, leading to higher deviations of localized porosity in the center region (Figure 3c).

More input views mitigate the particle adhesion phenomenon when synthetic data is in the input (Figure 4c). However, more artifacts due to particle stacking with increasing views is observed with real XCT data (blue box in Figure 5c). The cone beam of the X-ray source and sample shifting during imaging can lead to this observed flaw in terms of higher and unevenly distributed prediction errors on the surface when the input data is real radiographic images. In Tomo-NeRF and the artificial generator, we assume parallel-beam geometry for the flux of photons with the X-ray point source at an infinite distance from the testing object. In a real experiment, the distance between the X-ray source and the object is limited, forming a cone beam at an angle of 3.28°. The cone beam can distort the projection image away from the angle bisector of the cone. The higher energy for the photon flux near the angle bisector results in a brighter image (*i.e.*, overexposure). In addition to cone effect, slight misalignment during the experimental setup can result in part of the sample to be cut off in the field of view (orange box in Figure 5a). Particles obstructed or cut off from the field of view will not emerge in reconstructed experimental data (orange box in Figure 5b). The final challenge with experimental data is that Tomo-NeRF assumes that the sample rotates around a central axis. Any shift in the central axis will change the projection angle in the input data. Over long imaging experiments, where 1000 s of images are taken, it is common for some shifting to occur. One of the benefits of the sparse-view imaging approach is a decrease in imaging time and thus reduction of these artifacts.

According to the 2-D validation views and the novel views from the 3-D predictions, the validation views capture the input views structure (Figure 5d). More input views increase the sharpness of novel views, indicating a better reconstruction quality in the given projecting angle. There are visible differences between the 2-D predictions and the input views. It is due to the inaccurate assumption of the attenuation coefficient in particles and quartz containers. The incident energy of the polychromatic beam is uncertain, and the particles are made of mixtures with indeterminate proportions of materials. The model optimizes by minimizing the difference between the pixel predictions and the 2-D labels in a batch. Therefore, as long as the assumption of the attenuation coefficients is within the acceptable range and the 2-D predictions can reflect the main structure, the inaccurate assumption of the attenuation coefficient only has a limited effect on the 3D reconstruction results.

In addition to the abovementioned variations between the experiment and modeling, nonuniform information density within the 3D decoder (Figure 1) can also impact the

https://doi.org/10.1021/acsami.3c06291
ACS Appl. Mater. Interfaces 2023, 15, 35024−35033

reconstruction quality near the outer surfaces of the 3-D predictions. We visualize the prediction error of the six-view reconstructions for the synthetic irregular sphere sample (Figure 6a) and the real sample (Figure 6b) on the selected

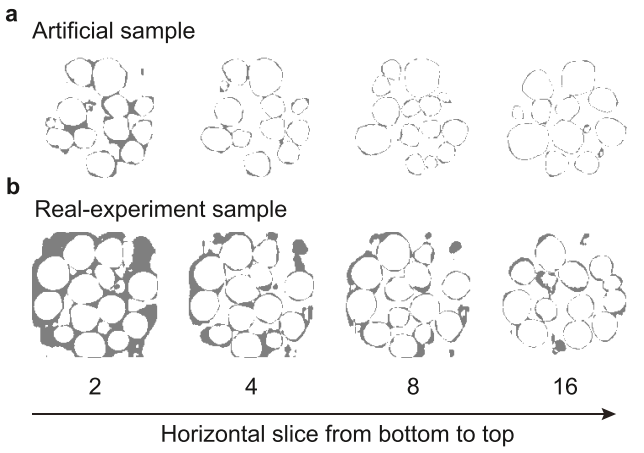

Figure 6. Visualization of prediction errors of synthetic data sample (a) (Experiment #2) and real sample (b) (Experiment #1) from bottom to top. For the slices closer to the center, the error mainly occurs near the particle surface. The information density gradient grows and is exacerbated as it propagates in the multilayer transposed convolution neural network. Decreases in prediction accuracy are observed near the top and bottom of the sample.

horizontal slices. The model is less likely to accurately discern and reconstruct the particles at the bottom of the sample which makes the particles look fused together. This issue is more exacerbated with real XCT data (Experiment #1, Figure 6b). When the distance from the bottom/top is more than four voxels, the reconstruction quality improves. During the transposed convolution operation, the voxels further away from the edge are able to receive a contribution from the adjacent voxel, *i.e.*, overlapping information.[2] The lack of overlapping information at the edge of the sample forms an information density gradient. The information density gradient becomes exacerbated as it propagates in the multilayer transposed convolution neural network. Furthermore, the particle projections near the top and bottom edges of the radiographic images are incomplete, thereby more irregular than the particles of the complete shape. The low information density and the more irregular shapes cause the low-quality reconstruction region near the top and bottom of the sample. This can be potentially resolved by subsequently feeding partially overlapping radiographic images into the model and then stitching together the central part of the reconstruction (with a higher prediction accuracy). The error map for the region away from the bottom/top shows that Tomo-NeRF manages to restore the position and general shape of the particles. However, errors primarily occur at the surface of the particles, indicating that the restoration of shape details is insufficiently accurate, particularly for the real-experiment sample.

CONCLUSIONS

Three-dimensional X-ray imaging is an important materials characterization approach which enables nondestructive and subsurface evaluation of a wide range of materials. There is a growing trend in 4-D imaging approaches which combine 3-D imaging with time. The latter is specifically useful for observing dynamic operating conditions also known as *in situ* or *operando*. One of the limitations in 4-D imaging is the need for 1000s of images which severely limits the temporal resolution of such a technique. Herein, we introduce a sparse-view reconstruction algorithm known as Tomo-NeRF. Tomo-NeRF is a physics-based learning approach which enables the reconstruction of 3-D images with limited 2-D views (<10 views). The results show the ability of Tomo-NeRF to reliably restore the structure of 3-D two-phase granular media from two-view 2-D radiographic images with a high structural similarity. Structural similarity approaching 0.9971 was obtained for real XCT images and 0.9973 as obtained for synthetic images with irregular particle shapes. The voxel-wise accuracy for real images (81.83−89.59%) is lower than synthetic images (86.40−95.37%). The deviation is likely because of experimental considerations which do not obey model assumptions (*e.g.*, low incident energy, differences in attenuation coefficients, polychromatic and cone beams, and sample shifting). Given that Tomo-NeRF involves the underlying physical principle of X-ray imaging and classifies each voxel into the appropriate phase, the model has the broad potential to readily adapt to other applications beyond granular structures (*e.g.*, fiber, pore, and even multiphase material) through transfer learning. Reconstruction of complex structures with high fidelity with single-digit radiographic images can significantly impact the temporal resolution of 4-D imaging. Future work aims to test the resiliency of these algorithms on dynamic imaging experiments.

ASSOCIATED CONTENT

Supporting Information

The Supporting Information is available free of charge at https://pubs.acs.org/doi/10.1021/acsami.3c06291.

Detailed architecture of the 2D image convolutional encoder and the 3D upsampling decoder (Section S1); procedure for data preprocessing and training (Section S2); formulations of loss functions (Section S3); detailed explanation and formulation for evaluation metrics (Section S4); comparison of 2D prediction in novel view with the ground truth for the synthetic sample of irregular shape (Experiment #2) (Figure S1); comparison of 2D prediction in novel view with the ground truth in full-view X-ray imaging experiment (Experiment #1) (Figure S2); particle network visualization comparison between ground truth and reconstruction for the synthetic sample of irregular shape (Experiment #2) (Figure S3); and particle network visualization comparison between ground truth and reconstruction in full-view X-ray imaging experiment (Experiment #1) (Figure S4) (PDF)

AUTHOR INFORMATION

Corresponding Author

Kelsey B. Hatzell − *Department of Mechanical and Aerospace Engineering, Princeton University, Princeton, New Jersey 08540, United States; Andlinger Center for Energy and the Environment, Princeton University, Princeton, New Jersey 08540, United States;* orcid.org/0000-0002-5222-7288; Email: kelsey.hatzell@princeton.edu

https://doi.org/10.1021/acsami.3c06291
ACS Appl. Mater. Interfaces 2023, 15, 35024−35033

Author

Yanjie Zheng − *Department of Mechanical and Aerospace Engineering, Princeton University, Princeton, New Jersey 08540, United States*

Complete contact information is available at: https://pubs.acs.org/10.1021/acsami.3c06291

Notes

The authors declare no competing financial interest.

■ ACKNOWLEDGMENTS

This material is based upon research supported by the Department of Energy, Solar Energy Technology Office under Award Number DE-EE0009385. K.B.H. and Y.Z. acknowledge support from the National Science Foundation under grant number 2140472.

■ REFERENCES

(1) Taillandier-Thomas, T.; Roux, S.; Hild, F. Soft Route to 4D Tomography. *Phys. Rev. Lett.* **2016**, *117*, No. 025501.

(2) Kench, S.; Cooper, S. J. Generating Three-Dimensional Structures From a Two-Dimensional Slice With Generative Adversarial Network-Based Dimensionality Expansion. *Nat. Mach. Intell.* **2021**, *3*, 299−305.

(3) Dong, J.; Fu, J.; He, Z. A Deep Learning Reconstruction Framework for X-Ray Computed Tomography With Incomplete Data. *PLoS One* **2019**, *14*, No. e0224426.

(4) Andersson, F. Fast Inversion of the Radon Transform Using Log-Polar Coordinates and Partial Back-Projections. *SIAM J. Appl. Math.* **2005**, *65*, 818−837.

(5) Withers, P. J.; Bouman, C.; Carmignato, S.; Cnudde, V.; Grimaldi, D.; Hagen, C. K.; Maire, E.; Manley, M.; Du Plessis, A.; Stock, S. R. X-Ray Computed Tomography. *Nat. Rev. Methods Primers* **2021**, *1*, No. R29.

(6) Quinto, E. T. In *An Introduction to X-Ray Tomography and Radon Transforms*, Proceedings of Symposia in Applied Mathematics, 2006; Vol. 63, p 1.

(7) Dixit, M. B.; Moreno, D.; Xiao, X.; Hatzell, M. C.; Hatzell, K. B. Mapping Charge Percolation in Flowable Electrodes Used in Capacitive Deionization. *ACS Mater. Lett.* **2019**, *1*, 71−76.

(8) Shen, L.; Zhao, W.; Capaldi, D.; Pauly, J.; Xing, L. A geometry-informed deep learning framework for ultra-sparse 3D tomographic image reconstruction. *Comput. Biol. Med.* **2022**, *148*, No. 105710.

(9) Shen, L.; Pauly, J.; Xing, L. NeRP: implicit neural representation learning with prior embedding for sparsely sampled image reconstruction. *IEEE Trans. Neural Networks Learn. Syst.* **2022**. DOI: 10.1109/TNNLS.2022.3177134.

(10) Shibata, H.; Hanaoka, S.; Nomura, Y.; Nakao, T.; Takenaga, T.; Hayashi, N.; Abe, O. On the Simulation of Ultra-Sparse-View and Ultra-Low-Dose Computed Tomography with Maximum a Posteriori Reconstruction Using a Progressive Flow-Based Deep Generative Model. *Tomography* **2022**, *8*, 2129−2152.

(11) Cha, E.; Chung, H.; Jang, J.; Lee, J.; Lee, E.; Ye, J. C. Low-Dose Sparse-View HAADF-STEM-EDX Tomography of Nanocrystals Using Unsupervised Deep Learning. *ACS Nano* **2022**, *16*, 10314−10326.

(12) Wu, Z.; Alorf, A.; Yang, T.; Li, L.; Zhu, Y. Robust X-ray Sparse-View Phase Tomography via Hierarchical Synthesis Convolutional Neural Networks. arXiv:1901.10644. arXiv.org e-Print archive, 2019. https://doi.org/10.48550/arXiv.1901.10644.

(13) Wang, G.; Ye, J. C.; De Man, B. Deep Learning for Tomographic Image Reconstruction. *Nat. Mach. Intell.* **2020**, *2*, 737−748.

(14) Ahishakiye, E.; Bastiaan Van Gijzen, M.; Tumwiine, J.; Wario, R.; Obungoloch, J. A Survey on Deep Learning in Medical Image Reconstruction. *Intell. Med.* **2021**, *1*, 118−127.

(15) Doh, W. H.; Papaefthimiou, V.; Zafeiratos, S. Applications of Synchrotron-Based X-Ray Photoelectron Spectroscopy in the Characterization of Nanomaterials. *Surf. Sci. Tools Nanomater. Charact.* **2015**, 317−366.

(16) Dong, X.; Vekhande, S.; Cao, G. In *Sinogram Interpolation for Sparse-View Micro-Ct With Deep Learning Neural Network*, Medical Imaging 2019: Physics of Medical Imaging; SPIE, 2019; Vol. 10948, pp 692−698.

(17) Lee, H.; Lee, J.; Cho, S. In *View-Interpolation of Sparsely Sampled Sinogram Using Convolutional Neural NetworkMedical Imaging 2017: Image Processing*; SPIE, 2017; Vol. 10133, pp 617−624.

(18) Lee, D.; Choi, S.; Kim, H.-J. High Quality Imaging From Sparsely Sampled Computed Tomography Data With Deep Learning and Wavelet Transform in Various Domains. *Med. Phys.* **2019**, *46*, 104−115.

(19) Gjesteby, L.; Yang, Q.; Xi, Y.; Zhou, Y.; Zhang, J.; Wang, G. In *Deep Learning Methods to Guide CT Image Reconstruction and Reduce Metal Artifacts*, Medical Imaging 2017: Physics of Medical Imaging; SPIE, 2017; Vol. 10132, pp 752−758.

(20) Lee, H.; Lee, J.; Kim, H.; Cho, B.; Cho, S. Deep-Neural-Network-Based Sinogram Synthesis for Sparse-View CT Image Reconstruction. *IEEE Trans. Radiat. Plasma Med. Sci.* **2019**, *3*, 109−119.

(21) Xie, S.; Zheng, X.; Chen, Y.; Xie, L.; Liu, J.; Zhang, Y.; Yan, J.; Zhu, H.; Hu, Y. Artifact Removal Using Improved GoogLeNet for Sparse-View CT Reconstruction. *Sci. Rep.* **2018**, *8*, No. 6700.

(22) Davoudi, N.; Deán-Ben, X. L.; Razansky, D. Deep Learning Optoacoustic Tomography With Sparse Data. *Nat. Mach. Intell.* **2019**, *1*, 453−460.

(23) Feng, J.; Teng, Q.; Li, B.; He, X.; Chen, H.; Li, Y. An End-to-End Three-Dimensional Reconstruction Framework of Porous Media From a Single Two-Dimensional Image Based on Deep Learning. *Comput. Methods Appl. Mechan. Eng.* **2020**, *368*, No. 113043.

(24) Gayon-Lombardo, A.; Mosser, L.; Brandon, N. P.; Cooper, S. J. Pores for Thought: Generative Adversarial Networks for Stochastic Reconstruction of 3D Multi-Phase Electrode Microstructures With Periodic Boundaries. *npj Comput. Mater.* **2020**, *6*, No. 82.

(25) Yu, A.; Ye, V.; Tancik, M.; Kanazawa, A. In *Pixelnerf: Neural Radiance Fields From One or Few Images*, Proceedings of the IEEE/CVF Conference on Computer Vision and Pattern Recognition, 2021; pp 4578−4587.

(26) Mildenhall, B.; Srinivasan, P. P.; Tancik, M.; Barron, J. T.; Ramamoorthi, R.; Ng, R. Nerf: Representing Scenes as Neural Radiance Fields for View Synthesis. *Commun. ACM* **2021**, *65*, 99−106.

(27) Yu, W.; Yang, K.; Bai, Y.; Yao, H.; Rui, Y.Visualizing and Comparing Convolutional Neural Networks. arXiv:1412.6631. arXiv.org e-Print archive, 2014. https://doi.org/10.48550/arXiv.1412.6631.

(28) Lenoir, N.; Bornert, M.; Desrues, J.; Bésuelle, P.; Viggiani, G. Volumetric Digital Image Correlation Applied to X-Ray Microtomography Images From Triaxial Compression Tests on Argillaceous Rock. *Strain* **2007**, *43*, 193−205.

(29) Stevenson, A. W.; Gureyev, T. E.; Paganin, D.; Wilkins, S.; Weitkamp, T.; Snigirev, A.; Rau, C.; Snigireva, I.; Youn, H.; Dolbnya, I.; et al. Phase-Contrast X-Ray Imaging With Synchrotron Radiation for Materials Science Applications. *Nucl. Instrum. Methods Phys. Res., Sect. B* **2003**, *199*, 427−435.

(30) Russo, P. *Handbook of X-ray Imaging: Physics and Technology*; CRC Press, 2017 ; pp 23−24.

(31) Akman, F.; Durak, R.; Turhan, M. F.; Kaçal, M. R. Studies on Effective Atomic Numbers, Electron Densities From Mass Attenuation Coefficients Near the K Edge in Some Samarium Compounds. *Appl. Radiat. Isot.* **2015**, *101*, 107−113.

(32) Dixit, M. B.; Zaman, W.; Bootwala, Y.; Zheng, Y.; Hatzell, M. C.; Hatzell, K. B. Scalable Manufacturing of Hybrid Solid Electrolytes With Interface Control. *ACS Appl. Mater. Interfaces* **2019**, *11*, 45087−45097.

(33) Narayan, S. The Generalized Sigmoid Activation Function: Competitive Supervised Learning. *Inf. Sci.* **1997**, *99*, 69−82.
(34) Rycroft, C. H.; Grest, G. S.; Landry, J. W.; Bazant, M. Z. Analysis of Granular Flow in a Pebble-Bed Nuclear Reactor. *Phys. Rev. E* **2006**, *74*, No. 021306.
(35) Jovanović, A.; Pezo, M.; Pezo, L.; Lević, L. DEM/CFD Analysis of Granular Flow in Static Mixers. *Powder Technol.* **2014**, *266*, 240−248.
(36) Möbius, M. E.; Lauderdale, B. E.; Nagel, S. R.; Jaeger, H. M. Size Separation of Granular Particles. *Nature* **2001**, *414*, 270.
(37) Sandnes, B.; Flekkøy, E.; Knudsen, H.; MÅløy, K.; See, H. Patterns and Flow in Frictional Fluid Dynamics. *Nat. Commun.* **2011**, *2*, No. 288.
(38) Cates, M. E.; Wittmer, J.; Bouchaud, J.-P.; Claudin, P. Jamming, Force Chains, and Fragile Matter. *Phys. Rev. Lett.* **1998**, *81*, 1841.
(39) Liu, A. J.; Nagel, S. R. Jamming Is Not Just Cool Any More. *Nature* **1998**, *396*, 21−22.
(40) Zhai, C.; Albayrak, N.; Engqvist, J.; Hall, S. A.; Wright, J.; Majkut, M.; Herbold, E. B.; Hurley, R. C. Quantifying Local Rearrangements in Three-Dimensional Granular Materials: Rearrangement Measures, Correlations, and Relationship to Stresses. *Phys. Rev. E* **2022**, *105*, No. 014904.
(41) Cheng, G. J.; Yu, A. Particle Scale Evaluation of the Effective Thermal Conductivity From the Structure of a Packed Bed: Radiation Heat Transfer. *Ind. Eng. Chem. Res.* **2013**, *52*, 12202−12211.
(42) Zheng, Y.; Hatzell, K. B. In *Thermal-Economic Optimization of Moving Packed Bed Particle-to-Sco2 Heat Exchanger Using Particle Swarm Optimization*, Energy Sustainability; American Society of Mechanical Engineers, 2021; p V001T02A010.
(43) Carbohsp. https://carboceramics.com/products/ceramic-proppant/carbohsp.
(44) Al Ibrahim, M. A.; Kerimov, A.; Mukerji, T.; Mavko, G. Particula: A Simulator Tool for Computational Rock Physics of Granular Media. *Geophysics* **2019**, *84*, F85−F95.
(45) de Jonge, M. D.; Tran, C. Q.; Chantler, C. T.; Barnea, Z.; Dhal, B. B.; Paterson, D.; Kanter, E. P.; Southworth, S. H.; Young, L.; Beno, M. A.; et al. Measurement of the X-Ray Mass Attenuation Coefficient and Determination of the Imaginary Component of the Atomic Form Factor of Tin Over the Energy Range of 29−60 keV. *Phys. Rev. A* **2007**, *75*, No. 032702.
(46) Caciuffo, R.; Melone, S.; Rustichelli, F.; Boeuf, A. Monochromators for X-Ray Synchrotron Radiation. *Phys. Rep.* **1987**, *152*, 1−71.

https://doi.org/10.1021/acsami.3c06291
ACS Appl. Mater. Interfaces 2023, 15, 35024−35033